

Electronic energy transport in nanoscale Au/Fe hetero-structures in the perspective of ultrafast lattice dynamics

Cite as: Appl. Phys. Lett. **120**, 092401 (2022); doi: [10.1063/5.0080378](https://doi.org/10.1063/5.0080378)

Submitted: 30 November 2021 · Accepted: 7 February 2022 ·

Published Online: 28 February 2022



View Online



Export Citation



CrossMark

M. Mattern,¹ A. von Reppert,¹  S. P. Zeuschner,^{1,2}  J.-E. Pudell,²  F. Kühne,³ D. Diesing,⁴  M. Herzog,¹  and M. Bargheer^{1,2,a)} 

AFFILIATIONS

¹Institut für Physik & Astronomie, Universität Potsdam, Karl-Liebknecht-Str. 24-25, 14476 Potsdam, Germany

²Helmholtz-Zentrum Berlin für Materialien und Energie, Wilhelm-Conrad-Röntgen Campus, BESSY II, Albert-Einstein-Strasse 15, 12489 Berlin, Germany

³Faculty of Physics and Center for Nanointegration (CENIDE), University of Duisburg-Essen, Lotharstrasse 1, 47057 Duisburg, Germany

⁴Faculty of Chemistry, University of Duisburg-Essen, Universitätsstr. 5, 45141 Essen, Germany

Note: This paper is part of the APL Special Collection on Ultrafast and Terahertz Spintronics.

^{a)}Author to whom correspondence should be addressed: bargheer@uni-potsdam.de

ABSTRACT

We study the ultrafast electronic transport of energy in a photoexcited nanoscale Au/Fe hetero-structure by modeling the spatiotemporal profile of energy densities that drives transient strain, which we quantify by femtosecond x-ray diffraction. This flow of energy is relevant for intrinsic demagnetization and ultrafast spin transport. We measured lattice strain for different Fe layer thicknesses ranging from few atomic layers to several nanometers and modeled the spatiotemporal flow of energy densities. The combination of a high electron-phonon coupling coefficient and a large Sommerfeld constant in Fe is found to yield electronic transfer of nearly all energy from Au to Fe within the first hundreds of femtoseconds.

Published under an exclusive license by AIP Publishing. <https://doi.org/10.1063/5.0080378>

Nanostructures composed of ferromagnetic transition metals and noble metals are ubiquitous in studies of ultrafast spin phenomena. Ultrafast demagnetization can be the consequence of intrinsic spin-flip scattering processes of electrons with phonons within the ferromagnet, or it depends on spin-currents across the interface to a metal without magnetic order.¹⁻⁷ These spin currents can be driven by photo-generated superdiffusive electrons, the spin-dependent shift of the Fermi level, or by the spin-Seebeck effect.⁸⁻¹⁰ All effects are connected to a redistribution of energy within the electron system.

Au/Fe bilayers prepared precisely in the way as the ones investigated here have been used in a large number of recent experiments aiming at fundamental understanding of spin dynamics.¹⁰⁻¹⁴ Time-resolved two-photon photoemission proved the injection of hot electrons into Au,^{11,12} whose spin-polarization leads to a transient magnetization in Au.^{13,14} In nanoscale Fe/Au/Fe hetero-structures, electrons propagating through the Au layer trigger perpendicular standing spin waves up to 0.6 THz via the spin-transfer torque.¹⁵ Various theoretical approaches discuss ballistic, superdiffusive, and diffusive components

of the electron transport,³⁻⁵ but the relative weight of non-equilibrium electrons and various thermal contributions depends on the details of the materials and the excitation conditions.⁸ A contribution of a ballistic channel for the electron transport was confirmed by second harmonic generation.¹⁰

The above studies exclusively focus on the electron and spin systems, although electron-phonon coupling influences their temperatures considerably. Especially in metal hetero-structures, the electronic transport and thus, the ultrafast magnetization dynamics can be adjusted by local material-specific variations of the electron-phonon coupling strength. Modeling of all-optical experiments in thicker bilayers can determine electron-phonon coupling constants and the spin-diffusion length.^{16,17} In this context, ultrafast x-ray diffraction (UXRD) provides a new perspective: It quantifies transient strain as a linear measure of the energy density in the physical subsystems of each material.¹⁸⁻²⁰ We have recently used the diffusive two-temperature model (TTM) to describe the unconventional heat transport in Pt/Cu/Ni hetero-structures, in which electrons propagate through a 100 nm thick Cu film

nearly without inelastic electron-phonon scattering events. This electronic excess energy is transported into the Ni layer at the backside of the multilayer stack, where it is dumped into the phonon system via the strong electron-phonon coupling.²¹ Such an UXR analysis can help to resolve discussions about proper modeling of the optical excitation of metallic bilayers, e.g., in experiments looking at the ultrafast demagnetization of Ni buried below a thick Au layer.^{22,23} We have clarified the excitation and ultrafast redistribution of electronic excitation in such hetero-structures with Au thicknesses in the single digit nanometer range by a modified two temperature model.²⁴

In this Letter, we discuss UXR experiments in Au/Fe bilayers, where the 30 nm Au film thickness is below the scattering length of Au electrons^{5,25} and the Fe layer thickness is varied from $d_{\text{Fe}} = 0$ to 20 nm across its electron scattering length scale [<2 nm (Ref. 26)]. The diffusive two-temperature model yields excellent agreement with the experimentally measured transient strain in Au with a fixed set of parameters for all Fe layer thicknesses. A rapid compression of the laser-excited Au film is the key feature of the measured strain for assessing the ultrafast electronic heat transport relevant to spin dynamics. Even when Fe is an order of magnitude thinner than the Au layer, the Au compression induced by the Fe expansion prevails over the intrinsic expansion of the Au layer. This is due to the flat 3d-bands of Fe at the Fermi-level with their large density of states $D(E_F)$, which is responsible for both the large electronic specific heat and strong electron-phonon interaction.²⁷ The majority of electronic energy optically excited in Au (and Fe) is quasi-instantaneously accepted in the electron system of the Fe layer, where it is rapidly converted to phonon energy. The strong electron-phonon coupling accelerates the flow of electronic thermal energy from Au to Fe, because it reduces the electron temperature and, thus, sustains the temperature gradient in the electronic system.

The Au/Fe bilayers are grown on MgO (001) substrates by molecular beam epitaxy. The Fe layer is prepared as a wedge with linearly varying thickness d_{Fe} by translating a shadow mask at constant velocity during deposition. The 20 nm thickness change extends over 4 mm, such that the x-ray focus of about 0.3 mm covers a thickness variation of 1.5 nm. Subsequently, 30 nm of Au are deposited both on bare MgO and on the Fe wedge [Fig. 1(b)]. Figure 1(a) compares the surface topography of a similar 40 nm Au film on bare MgO (left) to 40 nm Au with a 7 nm-Fe buffer layer (right). Atomic force microscopy (AFM) of the Au topography recorded on bare MgO exhibits a rather large roughness of $\Delta_{\text{rms}} = \pm 12$ nm, whereas the epitaxial growth on Fe yields much smoother Au films ($\Delta_{\text{rms}} = \pm 2$ nm). Reciprocal space maps [Figs. 1(c)–1(e)] reveal that a crystalline (001)-orientation of Au dominates on the Fe film, whereas on bare MgO the (111)-orientation prevails.

In the UXR experiment, the hetero-structure is excited from the Au-side by a 100 fs-long pump pulse with a central wavelength of 800 nm and a full-width half maximum spot size of $850 \times 1050 \mu\text{m}^2$. We probe the time-resolved expansion of the Au layer by the shift of the Bragg peak with the reciprocal space slicing method²⁸ at our laser-driven x-ray plasma source.²⁹ The incidence angle of the 8 keV x-ray pulses with a duration of 200 fs is kept fixed at the angles $\omega_{111} = 19.5^\circ$ [Fig. 1(c)] and $\omega_{002} = 22.7^\circ$ [Fig. 1(e)] to probe the two dominant crystalline orientations. For only few atomic layers of Fe, both orientations contribute considerably. In this case, we carried out cross-check experiments at $\omega = 21.0^\circ$ [Fig. 1(d)], where both peaks can be recorded simultaneously on the area detector.

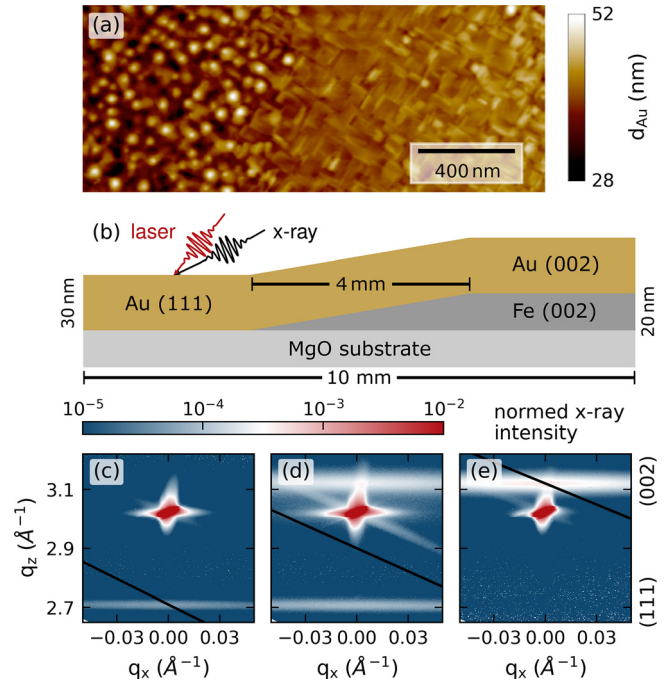


FIG. 1. (a) The AFM image shows the surface topography of a 40 nm Au film that was grown on bare MgO (left) and on 7 nm Fe on MgO (right). The Au film deposited on Fe has much better surface quality. Here, the transition from $d_{\text{Fe}} = 0$ to 7 nm occurs in a lateral extension of only 400 nm. (b) The schematic shows the wedge structure used for the time-resolved x-ray diffraction experiment. (c) The reciprocal space map recorded on a sample spot without Fe shows exclusively (111)-oriented Au at $q_z = 2.71 \text{ \AA}^{-1}$ in addition to the bright substrate peak. (d) Same at the onset of the Fe wedge, where both (111)- and (002)-oriented Au ($q_z = 3.12 \text{ \AA}^{-1}$) crystallites are observed. (e) On thicker Fe layers (002) prevails. The solid black lines indicate the subset of reciprocal space that is recorded on the area detector in the time-resolved measurements.

In Fig. 2, we show the average strain of the Au layer for a pump fluence of 5 mJ cm^{-2} at 300 K determined from the Bragg peak shift as a function of the delay time t between the pump and probe pulses

$$\eta_{\text{Au}}(t) = \frac{q_z(t < 0) - q_z(t)}{q_z(t < 0)}. \quad (1)$$

In the absence of a Fe buffer layer, we observe an expansion of Au that reaches its maximum 10 ps after excitation and displays a subsequent oscillation around a plateau-like strain of $\eta_{\text{Au}} = 0.75 \times 10^{-3}$. The oscillation originates from a propagating strain wave that is reflected both at the surface and the interface, where a part of the strain wave is transmitted into the substrate resulting in a decaying oscillation amplitude. The delay between two maxima of $2d_{\text{Au}}/v_s = 18$ ps corresponds to the propagation of the strain wave through the layer and back, and it is given by the layer thickness d_{Au} and the sound velocity v_s . In the presence of an additional Fe layer, we observe compression of Au within the first picoseconds. The dominating expansion of the Fe layer drives a compressive strain wave propagating into Au, resulting in initial compression, which becomes more pronounced with increasing Fe thickness. This strain wave is reflected at the surface and becomes expansive [Fig. 3(f)], resulting in a delayed plateau-like maximum of

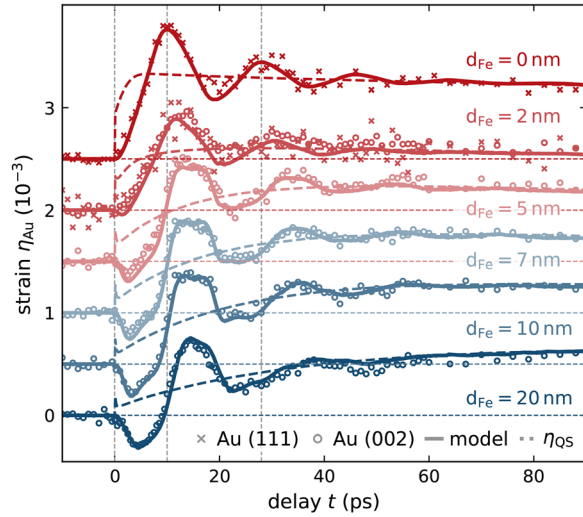


FIG. 2. Transient strain $\eta_{\text{Au}}(t)$ of the 30 nm Au film measured by UXRD for various Fe layer thicknesses from $d_{\text{Fe}} = 0$ to 20 nm at a pump fluence of 5 mJ cm^{-2} (data are offset for clarity). For $d_{\text{Fe}} = 2 \text{ nm}$, the measured transients for the (111)- and (002)-oriented crystallites agree. Solid lines represent the modeled transient strain of Au including coherent strain waves according to the elastic wave equation (3). Dashed lines represent the stationary solution of elastic wave equation (3) η_{QS} determined by the electron-phonon stress derived from the diffusive TTM [Eq. (2)].

the average Au strain. The subsequent propagation back and forth through the layer results in an oscillation of the mean strain as for bare Au according to the sound velocity of (002)-oriented Au. Superimposed on acoustic response, additional expansion indicates delayed slow heating of Au by the energy transport back from the buried Fe buffer layer (see dashed lines in Fig. 2).

We verify these conclusions by applying a diffusive TTM, which treats the heat transport by electrons and phonons separately via two differential equations coupled by the electron-phonon coupling using the modular PYTHON library `UDKMDSIM`,³⁰

$$\begin{aligned} C_{\text{el}}(T_{\text{el}}) \frac{\partial T_{\text{el}}}{\partial t} &= \frac{\partial}{\partial z} \left(\kappa_{\text{el}}(T_{\text{el}}, T_{\text{ph}}) \frac{\partial T_{\text{el}}}{\partial z} \right) + g(T_{\text{ph}} - T_{\text{el}}) + S_{\text{el}}(z), \\ C_{\text{ph}} \frac{\partial T_{\text{ph}}}{\partial t} &= \frac{\partial}{\partial z} \left(\kappa_{\text{ph}} \frac{\partial T_{\text{ph}}}{\partial z} \right) + g(T_{\text{el}} - T_{\text{ph}}). \end{aligned} \quad (2)$$

The model uses the thermophysical values for the heat conductivities $\kappa_{\text{el,ph}}$ of electrons and phonons, the corresponding specific heat C_{ph} , $C_{\text{el}} = \gamma^S T_{\text{el}}$, that contain the Sommerfeld constant γ^S , and the electron-phonon coupling constant g listed in Table I. We calculate the spatiotemporal dependence of the electron and phonon temperatures $T_{\text{el,ph}}(z, t)$ [Figs. 3(a) and 3(c)] and the corresponding energy densities $\rho_{\text{el,ph}}^Q(z, t)$ [Figs. 3(b) and 3(d)]. The spatial profile of the optical absorption $S_{\text{el}}(z)$ is calculated by an optical transfer matrix model.^{24,31} In order to compare the measured average strain to the modeled energy densities, we calculate the stress $\sigma_{\text{el,ph}}(z, t) = \Gamma_{\text{el,ph}} \cdot \rho_{\text{el,ph}}^Q(z, t)$ by material- and subsystem-specific Grüneisen constants $\Gamma_{\text{el,ph}}$. The elastic constant c_{33} connects the strain $\eta(z, t) = \partial u_{\perp} / \partial z$ [Fig. 3(f)] to the total laser-induced stress $\sigma_{\text{ext}}(z, t) = \sigma_{\text{el}}(z, t) + \sigma_{\text{ph}}(z, t)$ via the elastic wave equation of the displacement field $u_{\perp}(z, t)$,

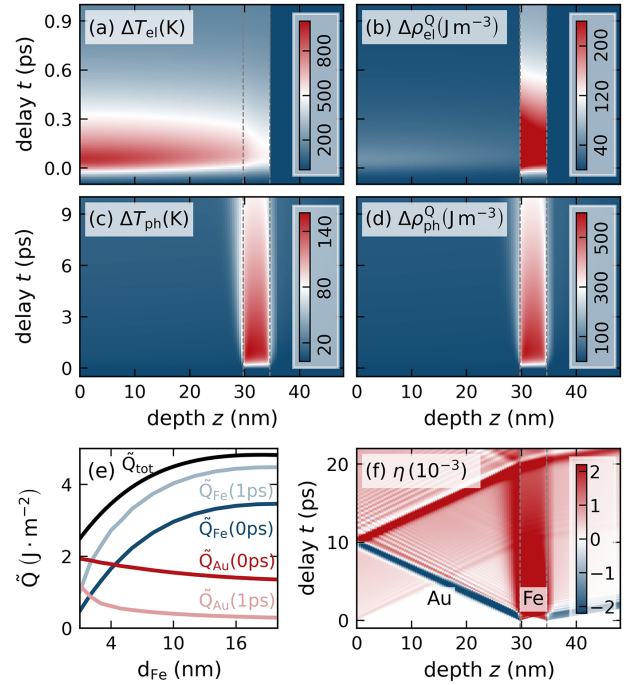


FIG. 3. Modeling of the photoexcited metal bilayer Au/Fe on MgO for Fe thickness $d_{\text{Fe}} = 5 \text{ nm}$: Heat maps of the spatiotemporal (a) electron temperature increase $\Delta T_{\text{el}}(z, t)$, (b) energy density increase in the electron system $\Delta \rho_{\text{el}}^Q(z, t)$, (c) phonon temperature increase $\Delta T_{\text{ph}}(z, t)$, and (d) phonon energy density increase $\Delta \rho_{\text{ph}}^Q(z, t)$. Panel (e) shows the energy per area directly after optical excitation [$\dot{Q}_{\text{Au,Fe}}(0 \text{ ps})$] and after electron-phonon equilibration in Fe [$\dot{Q}_{\text{Au,Fe}}(1 \text{ ps})$] as a function of d_{Fe} . (f) Lattice strain $\eta(z, t)$ determined from panels (b) and (d) and elastic wave equation (3).

$$\rho \frac{\partial^2 u_{\perp}}{\partial t^2} = \frac{\partial}{\partial z} \left(c_{33} \frac{\partial u_{\perp}}{\partial z} - \sigma_{\text{ext}}(z, t) \right). \quad (3)$$

We use the dynamical x-ray diffraction module of the toolbox³⁰ to model the transient peak shift and compare the extracted strain [Eq. (1)] to the experiment in Fig. 2. To illustrate the time-dependent energy densities $\rho_{\text{e,ph}}^Q$ in the Au film according to the TTM, we calculate the quasi-static expansion $\eta_{\text{QS}}(t) = \sigma_{\text{ext}}(t) / c_{33}$ from the spatially averaged stress $\sigma_{\text{ext}}(t) = \Gamma_{\text{el}} \rho_{\text{el}}^Q(t) + \Gamma_{\text{ph}} \rho_{\text{ph}}^Q(t)$ in Au. The quasi-static expansion is displayed by dashed lines in Fig. 2 and highlights the rise of the total stress in bare Au by electron-phonon coupling within few picoseconds and much slower heating of Au on a 30 ps timescale for a 20 nm Fe buffer layer.

We briefly discuss the parameters that are adjusted for modeling, but kept constant for all datasets in Fig. 2, where only the d_{Fe} is varied: We treat the incident fluence as an adjustable parameter of the model. Furthermore, we phenomenologically reduce the phonon conductivity in Au and Fe and include a typical interface resistance to MgO to match the Au expansion after tens of picoseconds.

Figure 3 exemplarily shows the modeled spatiotemporal temperatures and energy densities for electrons and phonons for a 5 nm-thin Fe layer. Figure 3(a) displays the equilibration of the electron

TABLE I. Thermophysical parameters of Au, Fe, and the MgO substrate taken from the literature. Values in brackets are optimized values for simulation.

	Au	Fe	MgO
γ^S (mJ cm ⁻³ K ⁻²)	0.07 ²⁷	1.02 ³²	...
C_{ph} (J cm ⁻³ K ⁻¹)	2.50 ³³	3.67 ³⁴	3.32 ³⁵
κ_{el} (W m ⁻¹ K ⁻¹)	313 ³⁶	65 ³⁷	...
κ_{ph} (W m ⁻¹ K ⁻¹)	5 ³⁶ (3)	7 ³⁷ (1)	50 ³⁸
g (PW m ⁻³ K ⁻¹)	25 ²⁷	2500 ^{39,40}	...
ρ (g cm ⁻³)	19.32	7.87	3.58
v_s (nm ps ⁻¹)	3.16 ^{a,41}	5.44 ⁴²	9.12 ⁴³
Γ_{el}	1.5 ⁴⁴	1.5	...
Γ_{ph}	3.0 ⁴⁴	1.7 ⁴⁵	1.6 ⁴⁶

^aFor (111)-oriented Au it is 3.45 nm ps⁻¹.

temperature throughout the Au/Fe bilayer within the electron-phonon coupling time in Fe ($\tau_{Fe} \approx 300$ fs). This short τ_{Fe} supports a strong temperature gradient within Fe and across the interface of the bilayer. The large electronic specific heat capacity in Fe localizes most of the deposited energy in the Fe electron system within the first 100 fs [Fig. 3(b)], before it is transferred to the energy density in the phonon system of Fe within τ_{Fe} [Fig. 3(d)]. As a result, nearly the complete optically deposited energy density is transferred to the Fe layer within the first picosecond. This is summarized for all d_{Fe} in Fig. 3(e). The phonon temperature and energy density maps [Figs. 3(c) and 3(d)] evidence a much slower increase in the phonon temperature in Au by near-equilibrium heat transport. This finding is consistent with similar experiments in Au/Ni bilayers.²⁴

For strain modeling, it is not relevant to distinguish superdiffusive from diffusive transport, since both occur faster than τ_{Fe} [Fig. 3(a)]. The large amount of the energy density stored in the Fe layer within the first picosecond induces an ultrafast expansion of Fe, which dominates over the intrinsic expansion of Au driven by the energy density in Au and, therefore, results in ultrafast compression of the Au layer. Only for Fe layer thicknesses $d_{Fe} \leq 2$ nm, the Au expansion prevails. However, even for the very thin Fe layer, the expansion of Au is reduced in comparison to Au on bare MgO. In essence, initial compression of Au (Fig. 2) evidence that energy absorbed by the Au electrons is transported into Fe within the first picosecond. While the increase in the energy densities $\Delta\rho^Q$ [Figs. 3(b) and 3(d)] determines the stress and, hence, the strain measured by UXRD, the modeling of the spatiotemporal electron temperature $T_{el}(z, t)$ [Fig. 3(a)] is relevant for ultrafast spin phenomena. In thermal equilibrium, these quantities are connected by $\Delta\rho_{el,ph}^Q = \int_{\Delta T} C_{el,ph}(T) dT$. In several experiments on ultrafast spin phenomena, the assumption of quasi-instantaneous formation of the Fermi distribution is a valid assumption.⁸ However, independent of this detail, modeling of the electronic transport should be consistent with the spatiotemporal dependence that we derive for $t \geq 1$ ps, i.e., after the electron-phonon coupling timescale τ_{Fe} .

We would like to elaborate on some details of the energy flow [Figs. 3(b) and 3(d)], since this can be highly relevant for understanding the thermodynamic perspective of ultrafast spin dynamics in metal hetero-structures. The electronic specific heat is dominated by the large density of states $D(E_F)$ at the Fermi-level that Fe owes to its flat 3d-bands. It yields a large Sommerfeld constant $\gamma^S = \pi^{2/3} k_B^2 D(E_F)$,

because of which the electronic specific heat $C_{el} = \gamma^S T$ of Fe is larger than the one of Au by the factor $f = \gamma_{Fe}^S / \gamma_{Au}^S = 15$. In other words, after tens of femtoseconds, the Fe layer that is 15 times thinner than the Au film still hosts the same energy. This imbalance of the energy density is aggravated by the relative ratio r of electron-phonon coupling g in the two films, $r = g_{Fe} / g_{Au} = 100$, which rapidly funnels the excess energy mainly into the phonon system of the Fe film. The modeling that is consistent with our experiment shows that for excitation of our hetero-structures with 800 nm pulses, the electron-phonon coupling is by far the dominant effect for increasing the energy density in Fe. Figure 3(e) highlights the considerable amount of energy that flows across the Au/Fe interface within the first picosecond (most of it even within the first 600 fs) for all thicknesses d_{Fe} . For the thinnest Fe layers below 4 nm, the energy transported from Au to Fe [$\bar{Q}_{Au}(0\text{ps}) - \bar{Q}_{Au}(1\text{ps}) = \bar{Q}_{Fe}(1\text{ps}) - \bar{Q}_{Fe}(0\text{ps})$] significantly decreases since the Fe layer is not able to accept more energy from the Au layer. Irrespective of the Fe thickness, the total electronic energy flow from Au to Fe could be considerably increased by exciting the Au layer at 400 nm, where the absorption in Au is strongly increased.²⁴

In conclusion, we experimentally showed that even an ultrathin Fe layer present as a buffer below an Au layer significantly changes the photoexcited strain and heat in the Au layer. A short-lived compression of the Au layer is observed, because the high electron-phonon coupling and Sommerfeld constant in Fe yield transfer of nearly all energy from Au to Fe according to a standard TTM. The model reproduces the thickness-dependence of the observed dynamics very well and sets rather strict boundaries on the spatiotemporal flow of electronic energy across the interface, which depends on the bilayer thicknesses. For distinguishing various demagnetization scenarios,⁸ such as spin-Seebeck effect, spin-voltage (spin dependent chemical potential), or the intrinsic demagnetization, it will be useful to consider our predicted electronic temperature profile $T_{el}(z, t)$ [Fig. 3(a)] and the total energy flow across the interface [Fig. 3(e)]. Spin-dynamics caused by non-equilibrium electron distributions, which only live for a short time after photo-excitation, should be carefully compared to the effect of mechanisms that can be described by local Fermi-distributions.

This work was funded by the Deutsche Forschungsgemeinschaft (DFG, German Research Foundation) via No. BA 2281/11-1 Project-No. 328545488 – TRR 227, project A10, and Project No. 278162697-SFB 1242.

AUTHOR DECLARATIONS

Conflict of Interest

The authors have no conflict of interest to disclose.

DATA AVAILABILITY

The data that support the findings of this study are available from the corresponding author upon reasonable request.

REFERENCES

- ¹E. Beaurepaire, J.-C. Merle, A. Daunois, and J.-Y. Bigot, "Ultrafast spin dynamics in ferromagnetic nickel," *Phys. Rev. Lett.* **76**, 4250 (1996).
- ²M. Hofherr, P. Maldonado, O. Schmitt, M. Berritta, U. Bierbrauer, S. Sadashivaiah, A. Schellekens, B. Koopmans, D. Steil, M. Cinchetti *et al.*, "Speed and efficiency of femtosecond spin current injection into a nonmagnetic material," *Phys. Rev. B* **96**, 100403 (2017).

- ³M. Battiato, K. Carva, and P. M. Oppeneer, "Superdiffusive spin transport as a mechanism of ultrafast demagnetization," *Phys. Rev. Lett.* **105**, 027203 (2010).
- ⁴M. Battiato, K. Carva, and P. M. Oppeneer, "Theory of laser-induced ultrafast superdiffusive spin transport in layered heterostructures," *Phys. Rev. B* **86**, 024404 (2012).
- ⁵D. M. Nenko, B. Rethfeld, and H. C. Schneider, "Particle-in-cell simulation of ultrafast hot-carrier transport in Fe/Au heterostructures," *Phys. Rev. B* **98**, 224416 (2018).
- ⁶G. Malinowski, F. Dalla Longa, J. Rietjens, P. Paluskar, R. Huijink, H. Swagten, and B. Koopmans, "Control of speed and efficiency of ultrafast demagnetization by direct transfer of spin angular momentum," *Nat. Phys.* **4**, 855–858 (2008).
- ⁷D. Rudolf, L.-O. Chan, M. Battiato, R. Adam, J. M. Shaw, E. Turgut, P. Maldonado, S. Mathias, P. Grychtol, H. T. Nembach *et al.*, "Ultrafast magnetization enhancement in metallic multilayers driven by superdiffusive spin current," *Nat. Commun.* **3**, 1037 (2012).
- ⁸A. Fognini, T. U. Michlmayr, A. Vaterlaus, and Y. Acremann, "Laser-induced ultrafast spin current pulses: A thermodynamic approach," *J. Phys.: Condens. Matter* **29**, 214002 (2017).
- ⁹G.-M. Choi, B.-C. Min, K.-J. Lee, and D. G. Cahill, "Spin current generated by thermally driven ultrafast demagnetization," *Nat. Commun.* **5**, 4334 (2014).
- ¹⁰A. Alekhin, I. Razdolski, N. Ilin, J. P. Meyburg, D. Diesing, V. Roddatis, I. Rungger, M. Stamenova, S. Sanvito, U. Bovensiepen *et al.*, "Femtosecond spin current pulses generated by the nonthermal spin-dependent Seebeck effect and interacting with ferromagnets in spin valves," *Phys. Rev. Lett.* **119**, 017202 (2017).
- ¹¹Y. Beyazit, J. Beckord, P. Zhou, J. Meyburg, F. Kühne, D. Diesing, M. Ligges, and U. Bovensiepen, "Local and nonlocal electron dynamics of Au/Fe/MgO (001) heterostructures analyzed by time-resolved two-photon photoemission spectroscopy," *Phys. Rev. Lett.* **125**, 076803 (2020).
- ¹²K. Bühlmann, G. Saerens, A. Vaterlaus, and Y. Acremann, "Detection of femtosecond spin injection into a thin gold layer by time and spin resolved photoemission," *Sci. Rep.* **10**, 12632 (2020).
- ¹³A. Alekhin, I. Razdolski, M. Berritta, D. Bürstel, V. Temnov, D. Diesing, U. Bovensiepen, G. Woltersdorf, P. M. Oppeneer, and A. Melnikov, "Magneto-optical properties of Au upon the injection of hot spin-polarized electrons across Fe/Au (0 0 1) interfaces," *J. Phys.: Condens. Matter* **31**, 124002 (2019).
- ¹⁴I. Razdolski, A. Alekhin, U. Martens, D. Bürstel, D. Diesing, M. Münzenberg, U. Bovensiepen, and A. Melnikov, "Analysis of the time-resolved magneto-optical Kerr effect for ultrafast magnetization dynamics in ferromagnetic thin films," *J. Phys.: Condens. Matter* **29**, 174002 (2017).
- ¹⁵I. Razdolski, A. Alekhin, N. Ilin, J. P. Meyburg, V. Roddatis, D. Diesing, U. Bovensiepen, and A. Melnikov, "Nanoscale interface confinement of ultrafast spin transfer torque driving non-uniform spin dynamics," *Nat. Commun.* **8**, 15007 (2017).
- ¹⁶K. Kang and G.-M. Choi, "Electron-phonon coupling parameter of ferromagnetic metal Fe and Co," *Material* **14**, 2755 (2021).
- ¹⁷K.-H. Ko and G.-M. Choi, "Optical method of determining the spin diffusion length of ferromagnetic metals," *J. Magn. Magn. Mater.* **510**, 166945 (2020).
- ¹⁸J. Pudell, A. von Reppert, D. Schick, F. Zamponi, M. Rössle, M. Herzog, H. Zabel, and M. Bargheer, "Ultrafast negative thermal expansion driven by spin disorder," *Phys. Rev. B* **99**, 094304 (2019).
- ¹⁹A. von Reppert, L. Willig, J.-E. Pudell, S. Zeuschner, G. Sellge, F. Ganss, O. Hellwig, J. Arregi, V. Uhlir, A. Crut *et al.*, "Spin stress contribution to the lattice dynamics of FePt," *Sci. Adv.* **6**, eaba1142 (2020).
- ²⁰A. von Reppert, M. Mattern, J.-E. Pudell, S. P. Zeuschner, K. Dumesnil, and M. Bargheer, "Unconventional picosecond strain pulses resulting from the saturation of magnetic stress within a photoexcited rare earth layer," *Struct. Dyn.* **7**, 024303 (2020).
- ²¹J.-E. Pudell, M. Mattern, M. Hehn, G. Malinowski, M. Herzog, and M. Bargheer, "Heat transport without heating?—An ultrafast x-ray perspective into a metal heterostructure," *Adv. Funct. Mater.* **30**, 2004555 (2020).
- ²²A. Eschenlohr, M. Battiato, P. Maldonado, N. Pontius, T. Kachel, K. Holdack, R. Mitzner, A. Föhlisch, P. M. Oppeneer, and C. Stamm, "Ultrafast spin transport as key to femtosecond demagnetization," *Nat. Mater.* **12**, 332–336 (2013).
- ²³A. Khorsand, M. Savoini, A. Kirilyuk, and T. Rasing, "Optical excitation of thin magnetic layers in multilayer structures," *Nat. Mater.* **13**, 101–102 (2014).
- ²⁴J. Pudell, A. Maznev, M. Herzog, M. Kronseder, C. Back, G. Malinowski, A. von Reppert, and M. Bargheer, "Layer specific observation of slow thermal equilibration in ultrathin metallic nanostructures by femtosecond x-ray diffraction," *Nat. Commun.* **9**, 3335 (2018).
- ²⁵R. Henriquez, M. Flores, L. Moraga, G. Kremer, C. González-Fuentes, and R. C. Munoz, "Electron scattering at surfaces and grain boundaries in thin Au films," *Appl. Surf. Sci.* **273**, 315–323 (2013).
- ²⁶J. Hong and D. L. Mills, "Spin dependence of the inelastic electron mean free path in Fe and Ni: Explicit calculations and implications," *Phys. Rev. B* **62**, 5589–5600 (2000).
- ²⁷Z. Lin, L. V. Zhigilei, and V. Celli, "Electron-phonon coupling and electron heat capacity of metals under conditions of strong electron-phonon non-equilibrium," *Phys. Rev. B* **77**, 075133 (2008).
- ²⁸S. Zeuschner, M. Mattern, J.-E. Pudell, A. von Reppert, M. Rössle, W. Leitenberger, J. Schwarzkopf, J. Boschker, M. Herzog, and M. Bargheer, "Reciprocal space slicing: A time-efficient approach to femtosecond x-ray diffraction," *Struct. Dyn.* **8**, 014302 (2021).
- ²⁹D. Schick, A. Bojahr, M. Herzog, C. v. K. Schmising, R. Shayduk, W. Leitenberger, P. Gaal, and M. Bargheer, "Normalization schemes for ultrafast x-ray diffraction using a table-top laser-driven plasma source," *Rev. Sci. Instrum.* **83**, 025104 (2012).
- ³⁰D. Schick, "UDKM1DSIM—A Python toolbox for simulating 1D ultrafast dynamics in condensed matter," *Comput. Phys. Commun.* **266**, 108031 (2021).
- ³¹K. Ohta and H. Ishida, "Matrix formalism for calculation of the light beam intensity in stratified multilayered films, and its use in the analysis of emission spectra," *Appl. Opt.* **29**, 2466–2473 (1990).
- ³²Z. Lin, L. V. Zhigilei, and V. Celli, "Electron-phonon coupling and electron heat capacity in metals at high electron temperatures," *Phys. Rev. B* **77**, 075133 (2008). Data for Fe are not available in the original manuscript but on the server of the authors: <https://faculty.virginia.edu/CompMat/electron-phonon-coupling/>.
- ³³Y. Takahashi and H. Akiyama, "Heat capacity of gold from 80 to 1000 K," *Thermochim. Acta* **109**, 105–109 (1986).
- ³⁴P. D. Desai, "Thermodynamic properties of iron and silicon," *J. Phys. Chem. Ref. Data* **15**, 967–983 (1986).
- ³⁵T. Barron, W. Berg, and J. Morrison, "On the heat capacity of crystalline magnesium oxide," *Proc. R. Soc. London, Ser. A* **250**, 70–83 (1959).
- ³⁶N. Stojanovic, D. Maithripala, J. Berg, and M. Holtz, "Thermal conductivity in metallic nanostructures at high temperature: Electrons, phonons, and the Wiedemann-Franz law," *Phys. Rev. B* **82**, 075418 (2010).
- ³⁷N. Bäcklund, "An experimental investigation of the electrical and thermal conductivity of iron and some dilute iron alloys at temperatures above 100 K," *J. Phys. Chem. Solids* **20**, 1–16 (1961).
- ³⁸A. J. Slifka, B. J. Filla, and J. Phelps, "Thermal conductivity of magnesium oxide from absolute, steady-state measurements," *J. Res. Natl. Inst. Stand. Technol.* **103**, 357 (1998).
- ³⁹N. Medvedev and I. Milov, "Electron-phonon coupling in metals at high electronic temperatures," *Phys. Rev. B* **102**, 064302 (2020).
- ⁴⁰D. Zahn, F. Jakobs, H. Seiler, T. A. Butcher, D. Engel, J. Vorberger, U. Atxitia, Y. W. Windsor, and R. Ernstorfer, "Intrinsic energy flow in laser-excited 3D ferromagnets," *Phys. Rev. Res.* **4**(1), 013104 (2022).
- ⁴¹Y. Chang and L. Himmel, "Temperature dependence of the elastic constants of Cu, Ag, and Au above room temperature," *J. Appl. Phys.* **37**, 3567–3572 (1966).
- ⁴²J. Rayne and B. Chandrasekhar, "Elastic constants of iron from 4.2 to 300 K," *Phys. Rev.* **122**, 1714 (1961).
- ⁴³M. A. Durand, "The temperature variation of the elastic moduli of NaCl, KCl and MgO," *Phys. Rev.* **50**, 449 (1936).
- ⁴⁴M. Nicoul, U. Shymanovich, A. Tarasevitch, D. von der Linde, and K. Sokolowski-Tinten, "Picosecond acoustic response of a laser-heated gold-film studied with time-resolved x-ray diffraction," *Appl. Phys. Lett.* **98**, 191902 (2011).
- ⁴⁵F. Nix and D. MacNair, "The thermal expansion of pure metals: Copper, gold, aluminum, nickel, and iron," *Phys. Rev.* **60**, 597 (1941).
- ⁴⁶G. White and O. Anderson, "Grüneisen parameter of magnesium oxide," *J. Appl. Phys.* **37**, 430–432 (1966).